PROGRESS IN PHOTOVOLTAICS: RESEARCH AND APPLICATIONS
Prog. Photovolt: Res. Appl. (2011)
Published online in Wiley Online Library (wileyonlinelibrary.com). DOI: 10.1002/pip.1126

RESEARCH ARTICLE

Synchrotron-based microprobe investigation of impurities in raw quartz-bearing and carbon-bearing feedstock materials for photovoltaic applications

Sarah Bernardis[1]*, Bonna K. Newman[1], Marisa Di Sabatino[2,3], Sirine C. Fakra[4], Mariana I. Bertoni[1], David P. Fenning[1], Rune B. Larsen[5] and Tonio Buonassisi[1]

[1] Massachusetts Institute of Technology, Cambridge, MA 02139, USA
[2] Department of Materials Science and Engineering, Norwegian University of Science and Technology, 7491 Trondheim, Norway
[3] SINTEF Materials and Chemistry, 7465 Trondheim, Norway
[4] Advanced Light Source, Lawrence Berkeley National Laboratory, Berkeley, CA 94720, USA
[5] Department of Geology and Mineral Resources Engineering, Norwegian University of Science and Technology, 7491 Trondheim, Norway

ABSTRACT

Using synchrotron-based analytical microprobe techniques, we determine micrometer-scale elemental composition, spatial distribution, and oxidation state of impurities in raw feedstock materials used in the photovoltaic industry. Investigated Si-bearing compounds are pegmatitic quartz, hydrothermal quartz, and quartzite. Micrometer-scale clusters containing Fe, Ti, and/or Ca are frequently observed at structural defects in oxidized states and in bulk concentrations equivalent to inductively coupled plasma mass spectroscopy measurements. Investigated C-bearing compounds are pine wood, pine charcoal, and eucalyptus charcoal. Clustered metals are observed only in the charcoal samples. Impurity clustering implies that industrial processing could be adapted to take advantage of this "natural gettering" phenomenon, expanding the usable range of raw feedstock materials to dirtier, cheaper, and more abundant ones, currently underexploited for solar-grade silicon production. Copyright © 2011 John Wiley & Sons, Ltd.

***Correspondence**
Sarah Bernardis, Massachusetts Institute of Technology, Cambridge, MA 02139, USA.
E-mail: bernardis@alum.mit.edu

Received 3 February 2011; Revised 25 March 2011

1. INTRODUCTION

Impurities degrade silicon-based solar cell performance, reducing minority carrier diffusion length [1,2] and power output [3,4]. To avoid the negative effects of impurities, photovoltaic devices have traditionally been fabricated using high-purity (9N) electronics-grade silicon. However, their high costs and limited availability led to exploring alternatives termed solar-grade silicon (SoG-Si, 6N purity [5]), including modified Siemens processes and upgraded metallurgical-grade silicon (UMG-Si) [6].

Impurities in SoG-Si originate from multiple sources, including raw feedstock materials, arc-furnace lining, electrodes, and handling. We focus on Si-bearing and C-bearing raw feedstocks because these are unavoidable and natural reactants; furthermore, they can be among the dominant impurity contributors in SoG-Si. A deeper understanding of the microscopic distributions and oxidation states of these impurities in raw feedstock materials could assist in developing more competitive and efficient refining techniques, thus improving existing processes and widening the usable feedstock to less pure materials.

Our current study focuses on three major impurities of interest: Fe, Ti, and Ca. Iron is a fast-diffusing transition metal in silicon [7] with a strong negative impact on cell performance [1,8]. Titanium has lower diffusivity and solubility than iron [7], yet it limits more severely cell efficiency [1]. Calcium is not considered an impurity with strong electrical activity [9], and its action in purifying silicon is actually sought during slagging [10]. However, ongoing investigations indicate that selected phase transitions in the Ca–O system can disrupt silicon refining and ingot crystallization [11,12].

We use synchrotron-based X-ray analytical microprobe techniques to elucidate the microscopic distributions and chemical states of impurity-rich particles in aforementioned raw feedstock materials used for SoG-Si production. We find that impurities naturally segregate to form larger clusters or distinct phases of impurities in oxidized states at grain boundaries and other structural defects. However, in the current refining process, this natural segregation is negated, and these high concentrations of impurities are introduced into the furnace. New chemical, biological, or physical processes could be developed to take advantage of the natural segregation occurring in these materials, leading to an upstream solution for removing detrimental impurities in silicon for solar cells.

2. MATERIALS AND METHODS

2.1. Materials

Three quartz-bearing and four carbon-bearing feedstocks were analyzed. Impurity distributions in Si-bearing feedstock materials are governed by geological formation processes, summarized below and described in detail in Refs [13,14]. Raw feedstock choice is limited by the availability of relevant industrial samples rather than completeness.

Pegmatitic quartz is an igneous rock-forming mineral. Quartz crystallizes from 500°C to 700 °C in a volatile-rich silicate melt yielding fast, long-range diffusion of Si and O ions but few crystal nuclei, resulting in large quartz crystals (centimeter-scale to micrometer-scale) [13]. The same long-range diffusion also encourages foreign elements (i.e., potentially harmful impurities) to form distinct phases rather than being incorporated in the quartz lattice [13,14].

Hydrothermal quartz precipitates directly from aqueous fluids rich in salts, silica ions, and minor compounds. The hydrothermal fluids govern impurity concentration, which is found to range from less than 40 mg/g to hundreds [15]. Occasionally, low-temperature (300–400°C) hydrothermal fluids infiltrate previously crystallized quartz, whether pegmatitic, hydrothermal, or metamorphic, re-crystallizing it to excellent quality [13,14].

Quartzite is formed by metamorphosis, typically of sedimentary sand deposits. Unconsolidated quartz-rich sediments are buried and heated during orogenic events and amalgamated into a solid rock at temperatures of 300–700°C and pressures higher than 4000 bars [16]. Contrary to hydrothermal and pegmatitic quartz, foreign minerals comprising several per cents of the sediments also re-crystallize during this process, resulting in high impurity concentrations [16], both in the quartz lattice structure and as minute minerals along grain boundaries.

For optical microscopy, standard 30-μm thick petrographic sections of the Si-bearing compounds were prepared by Spectrum Petrographics, Inc. (Vancouver, WA, USA). For synchrotron-based X-ray microprobe investigations, Si-bearing compounds were cut with a diamond saw blade, polished with SiC paper, and cleaned in ultrasonic baths of acetone, ethanol, and isopropanol. Samples were stored in a clean (metal-free) environment until measurements at the synchrotron.

We investigated four carbon-bearing raw feedstocks: pine wood, pine charcoal, Brazilian eucalyptus charcoal [17], and an Indonesian charcoal mixture of several wood types [18]. The pine wood chip is the precursor of the pine charcoal; details of an analogous charcoal formation process can be found in [18].

The pine wood and pine charcoal were provided in small cubes (1 cm^3); these were cleaved along the pine veins in a clean, metal-free environment, followed by immediate X-ray microprobe measurements to avoid contamination. The Indonesian and Brazilian charcoals were provided in small chunks; one piece per charcoal batch demonstrating a flat area was used for synchrotron measurements.

2.2. Characterization techniques

2.2.1. Optical microscopy

Thirty-micrometer thin sections of quartz-bearing compounds were studied by reflected and transmitted cross-polarized light microscopy using a Nikon Eclipse E600 microscope with LUPan objectives at 50× total magnification (Nikon Instruments Inc., Melville, NY, USA). Sample homogeneity, texture, grain-size distribution, and presence of fluid and solid inclusions (i.e., foreign minerals) were evaluated.

2.2.2. X-ray microprobe

To determine impurity particle size, spatial distribution, and elemental composition, we employed micro-focused X-ray fluorescence (μ-XRF) mapping and X-ray absorption near-edge structure (μ-XANES) spectroscopy. These synchrotron-based "photon in, photon out" techniques have low Bremsstrahlung background providing orders of magnitude higher bulk sensitivity than electron-based techniques [19,20] and are capable of characterizing the spatial distribution and chemical nature of nanometer-sized clusters within cubic millimeters of insulating material [21]. In the past, they have been successfully applied to study elemental distributions in non-conductive rocks and minerals [22], wood samples [23], as well as metallic impurities in multicrystalline silicon solar cell materials [24,25].

For large-area μ-XRF maps, we used Beamline 10.3.2 of the Advanced Light Source (ALS) at Lawrence Berkeley National Laboratory (Berkeley, CA, USA) with a 7.3 and 10 keV incident X-ray beam, a $6 \times 6\ \mu m^2$ spot size, and a seven-element germanium detector [26]. For higher-resolution maps, we used Beamline 2-ID-D at the Advanced Photon Source at Argonne National Laboratory (Argonne, IL, USA), with 10 keV incident beam, a 200 nm diameter spot, and a silicon drift detector [27]. To convert μ-XRF counts into micrograms per square centimeter ($\mu g/cm^2$), we measured two National Institute of Standards

and Technology (NIST) standards (NIST 1833 and NIST 1832). Volumetric concentrations ($\mu g/cm^3$) were obtained by dividing the map concentration ($\mu g/cm^2$) by the X-ray attenuation length (cm). A detailed quantitative analysis description can be found in [28]. No volumetric concentration could be estimated for the C-bearing compounds, as the conversion between areal and volumetric concentrations requires knowledge of matrix density and porosity.

The oxidation states of particles rich in Fe, Ti and Ca were determined by μ-XANES measurements at ALS Beamline 10.3.2 using a Si(111) monochromator with energy resolution less than 1 eV [26]. K-edge absorption spectra were collected in fluorescence mode, up to 300 eV above the edge, on several spots of interest. Spectra were calibrated using elemental foil first derivative set at 7110.75 eV (Fe), 4966.40 eV (Ti), and 4132.2 eV (Sb for Ca) [29]. Spectra were deadtime corrected, pre-edge background subtracted, and post-edge normalized using standard procedures [30]. Least-square linear combination fitting of the Fe K-edge spectra was performed in the 7010–7410 eV range using a large public database of well-characterized Fe X-ray absorption spectra standards [31], and fine features in the pre-edge region of each spectrum were used to infer oxidation state [31–34]. All data processing was performed using a suite of custom programs, based on LabView (National Instruments, Austin, TX, USA) software, available at the beamline.

2.2.3. Bulk analysis

Bulk concentrations of trace elements were measured by inductively coupled plasma mass spectroscopy (ICP-MS) and atomic emission spectroscopy. Measurements were performed by Metron Tech (Burlingame, CA, USA) on the same specimens analyzed by X-ray microprobe techniques. Before dissolution, quartz samples were treated with an acidic etch to remove surface contamination (~2 μm). For all feedstock materials, the measurements were repeated twice, and the average is provided. The measurement detection limit is 2 ng/g for Fe, 1 ng/g for Ti, and 2 ng/g for Ca. Measurement error is estimated to be ±50% and ±10%, respectively, for values 5 and 10 times higher than the detection limit.

3. RESULTS

3.1. Optical microscopy

Pegmatitic quartz shows millimeter-wide milky-white colored bands separated by transparent zones, indicating trails of secondary fluid inclusions (Figure 1a). Grains are centimeter-sized; structural defects, fractures, and grain boundaries are visible, whereas other optically identifiable minerals are rare.

Hydrothermal quartz has a milky-white color because of a high concentration of microscopic fluid inclusions with aqueous saline solutions. A variety of grain sizes are observed (Figure 1b); polygonal grains with subgrain formation (i.e., finer-grained crystals along grain boundaries) and grain overgrowth imply partial re-crystallization. Inter-granular and intra-granular fractures are common; other minerals (e.g., feldspars) are rarely visible.

Quartzite is brown; quartz crystals are medium grained with discernible grains of foreign minerals (Figure 1c); copresence of well-defined rounded or sharp edges and grain overgrowth implies local re-crystallization. Micas and other minerals are visible along grain boundaries.

3.2. Elemental analysis

3.2.1. Iron

Fe clusters are detected by μ-XRF in all Si-bearing feedstocks (Figure 2, first column) and in some of the C-bearing compounds (Figure 3, first column). In pegmatitic quartz, dispersed Fe particles in what is likely an intergranular region are determined by μ-XANES to be ferric (Fe^{3+}) species (Figure 4a). In the hydrothermal quartz, Fe particles are also distributed throughout the map; comparison with the Ca map suggests that Fe is located predominantly at grain boundaries. μ-XANES reveals that these particles are ferrous (Fe^{2+}) species (Figure 4b). In quartzite, Fe is present in filament-like nets along grain boundaries (Figure 5a) and grain-size inclusions (Figure 2). According to μ-XANES analyses, quartzite contains both ferric and ferrous iron-rich clusters (Figure 4c). ICP-MS measurements indicate bulk Fe concentrations at or below 20 mg/g for pegmatitic and

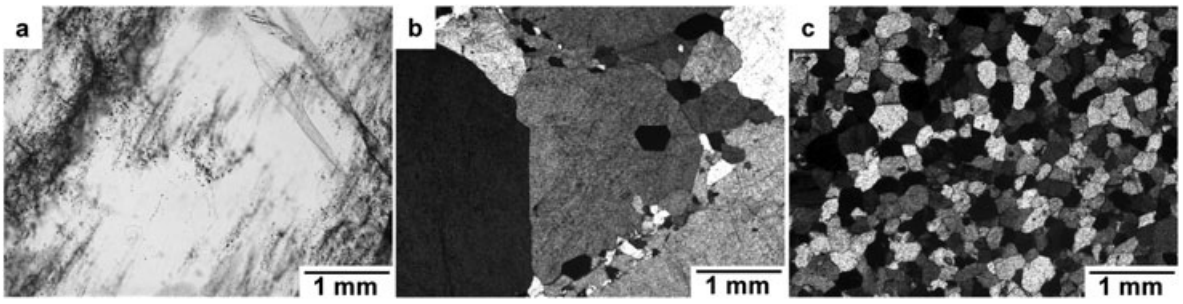

Figure 1. Representative optical micrographs in normal (a) and cross-polarized light (b, c) of the silicon-bearing samples: (a) pegmatitic quartz; (b) hydrothermal quartz; and (c) quartzite.

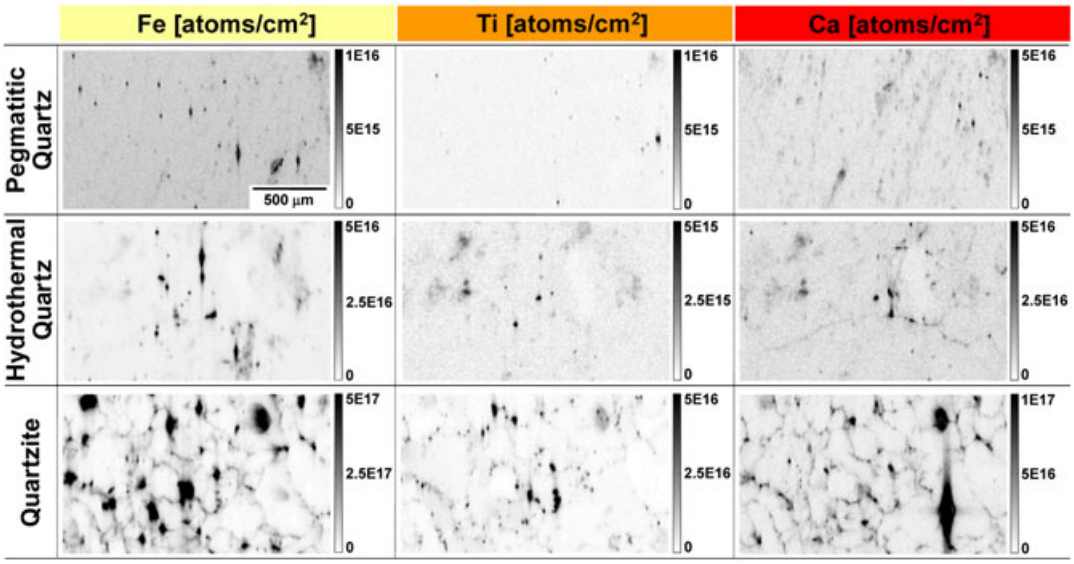

Figure 2. Micro-focused X-ray fluorescence maps of silicon-bearing compounds used during silicon refining. Impurities are predominantly seen in clusters, which tend to decorate structural defects. Intensity scale bars [atoms/cm^2] are optimized for maximum contrast.

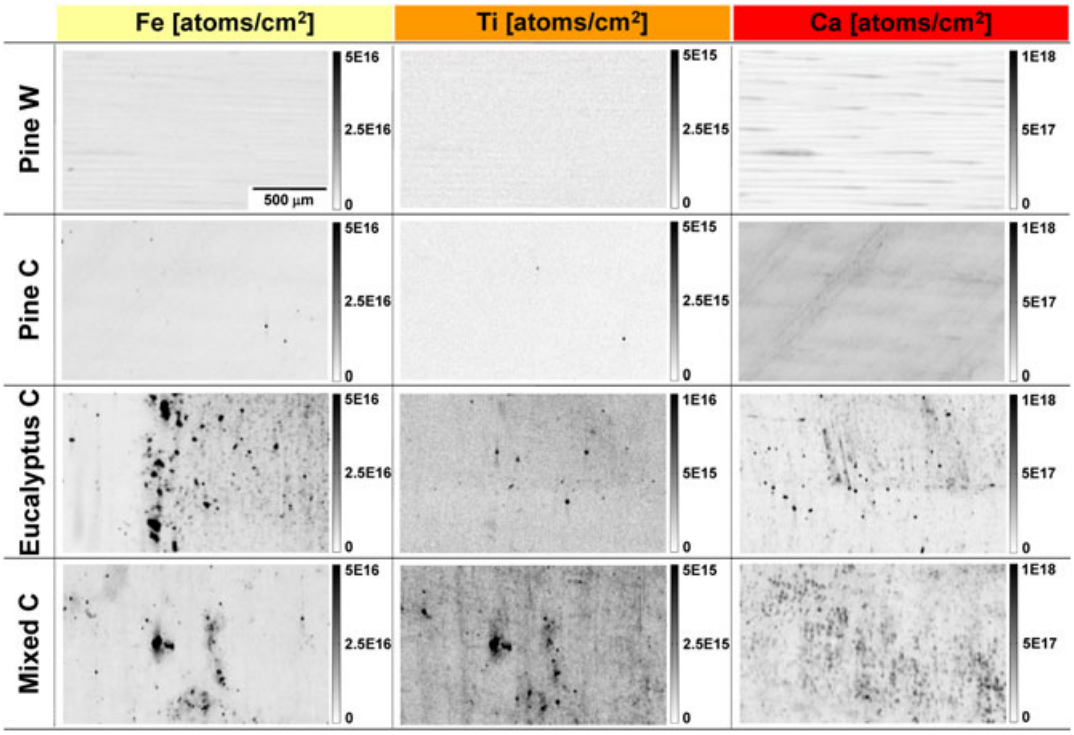

Figure 3. Micro-focused X-ray fluorescence maps of carbon-bearing compounds used during silicon refining ("W" stands for woodchip and "C" for charcoal). Impurity clusters can be observed in charcoal samples. Intensity scale bars [atoms/cm^2] are optimized for maximum contrast.

hydrothermal quartz and above 1000 mg/g for quartzite (Figure 6a). Bulk Fe concentrations calculated from µ-XRF maps are comparable to ICP-MS results within a factor of four, suggesting that regions scanned by µ-XRF are representative of each sample as a whole and that the majority of Fe is contained in second-phase particles.

Fe appears homogeneously distributed along the wood veins in both the pine woodchip and the pine charcoal

DOI: 10.1002/pip

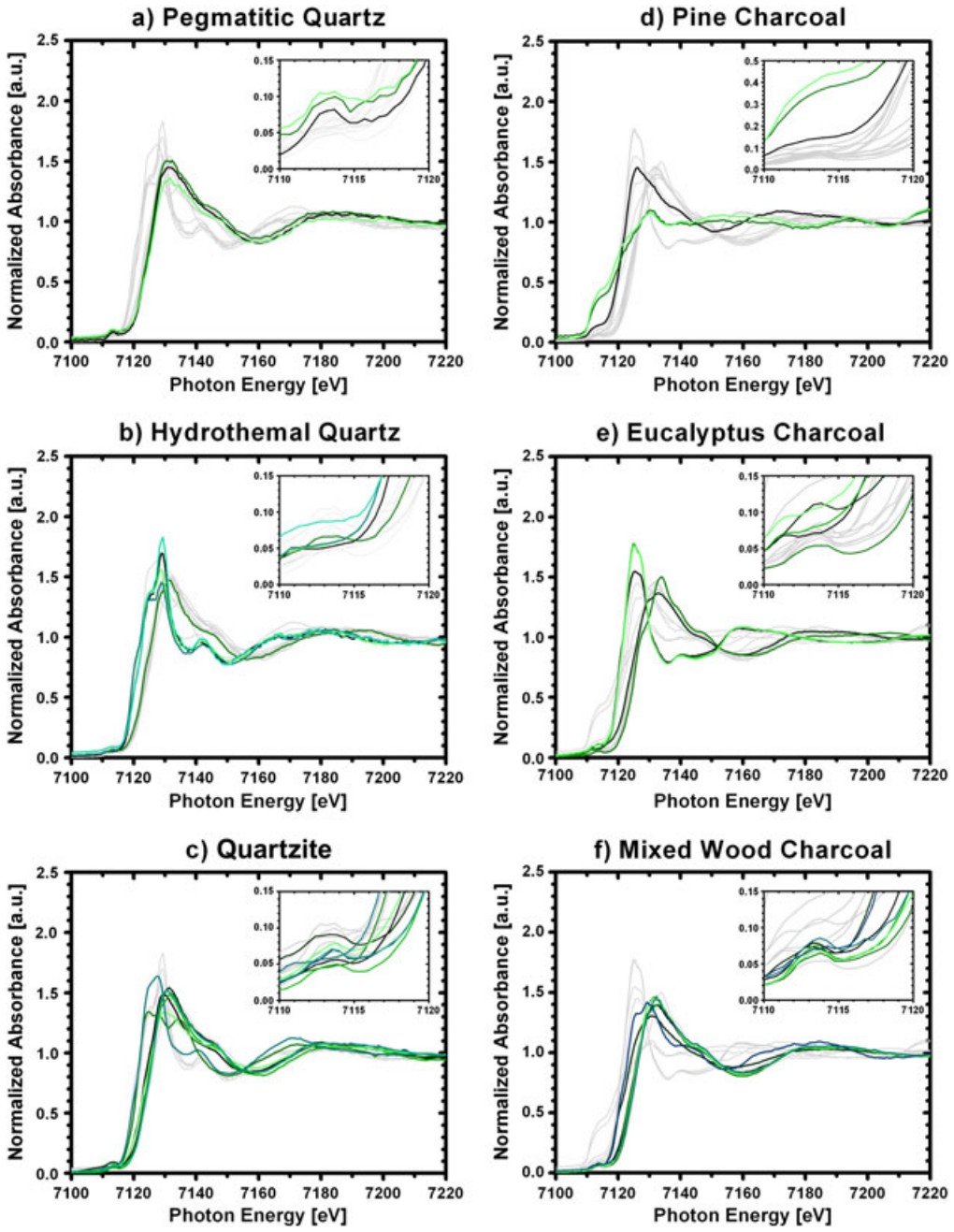

Figure 4. Fe K-edge X-ray absorption near-edge structure spectra of the Si-bearing (a–c) and C-bearing (d–f) feedstock materials. Fe^0 peaks at 7110 eV (d), Fe^{2+} at 7111.5 eV (b, c, e), and Fe^{3+} at 7113 eV (a, c, d, e, f); peak splitting between 7111.5 and 7113 eV indicates 2^+ and 3^+ oxidation state mixing (c, f).

(Figure 3, first column). Fe-rich particles are observed in each of the charcoal samples: in pine charcoal, they are either metallic or ferric (Figure 4d); in eucalyptus charcoal, they are ferric, ferrous, and a mixture of the two (Figure 4e); in mixed charcoal, they are predominantly ferric with a few mixed ferric–ferrous particles (Figure 4f). ICP-MS measurements (Figure 6b) indicate Fe concentrations in low mg/g for the pine woodchip, pine charcoal, and eucalyptus charcoal and an order of magnitude higher for the mixed-wood charcoal.

3.2.2. Titanium

Ti-rich particles are present in each of the Si-bearing feedstocks (Figure 2, second column). In the hydrothermal quartz, some clusters are co-located with Ca along structural defects. In the quartzite, Ti forms circular

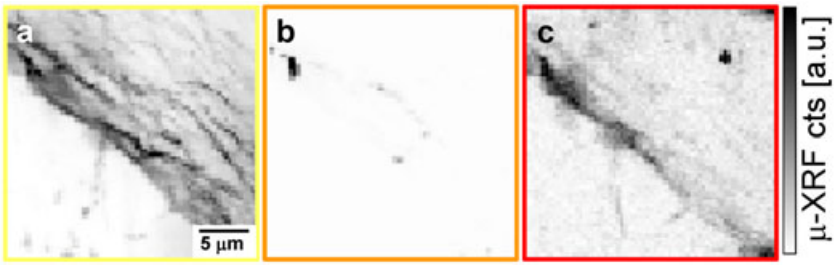

Figure 5. Micro-focused X-ray fluorescence map of a grain boundary in quartzite showing distribution of (a) Fe, (b) Ti, and (c) Ca.

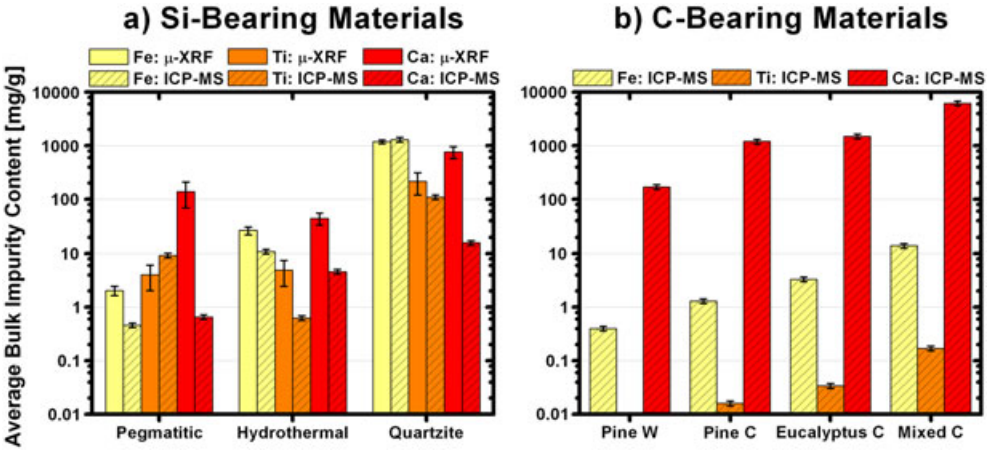

Figure 6. Impurity concentration of iron (yellow), titanium (orange), and calcium (red) in the (a) Si-bearing and (b) C-bearing compounds ("W" stands for woodchip and "C" for charcoal). Results obtained from micro-focused X-ray fluorescence (μ-XRF) measurements (full color) are compared to inductively coupled plasma mass spectroscopy (ICP-MS) analysis (textured color).

particles along grain boundaries; Figure 3b shows such a nucleus in a high-resolution μ-XRF map. Good agreement between ICP-MS and μ-XRF measurements of bulk Ti is observed (Figure 6a), with Ti content increasing from hydrothermal and pegmatitic to quartzite.

Although μ-XRF detects no Ti-rich particles in either of the pine samples (Figure 3, second column), a low, homogeneous Ti signal follows the wood veins. ICP-MS confirms low bulk Ti concentrations (Figure 6b) in these samples. Ti-rich particles are observed by μ-XRF in the eucalyptus and mixed charcoal samples; ICP-MS correspondingly detects relatively higher bulk Ti concentrations. The oxidation state of Ti determined by μ-XANES is inconclusive in the eucalyptus charcoal; Ti^{4+} is found in the mixed charcoal.

3.2.3. Calcium

In the pegmatitic quartz, Ca (Figure 2, third column) is closely correlated with the distribution of fluid inclusions. In the hydrothermal quartz, Ca segregates to a textural feature traversing the μ-XRF map, likely a structural defect such as a grain boundary. In quartzite, like Fe, Ca follows grain boundaries in a continuous layer, rather than forming discrete clusters as seen for Ti. For all samples, μ-XANES analyses reveal Ca^{2+}. ICP-MS concentration measurements (Figure 6a) reveal an increasing bulk Ca concentration from hydrothermal to pegmatitic quartz to quartzite. However, these bulk measurements are systematically lower than those determined by μ-XRF (Figure 6a), possibly a result of sampling bias and/or handling.

In both pine samples (Figure 3, third column), Ca is distributed along wood veins. In eucalyptus and mixed-wood charcoal, discrete particles containing Ca^{2+} are detected. Bulk Ca concentrations (ICP-MS, Figure 6b) range from hundreds to thousands mg/g for all species, with lowest levels in the pine woodchip.

3.2.4. Elemental co-location and other impurities

Impurity co-location, inferred via pixel-by-pixel analyses of the μ-XRF maps, can result from interactions (e.g., free-energy minimization via precipitation with other elements) or coincidence (e.g., preferred precipitation of two or more elements at the same heterogeneous nucleation site).

In the pegmatitic quartz, co-location of Ti, Ca, and Fe is occasionally observed. It is observed that Ti and Ca interact (e.g., $CaTiO_3$ can form in some Fe-rich minerals).

Most particles contain Ca, Cr, Fe, Ni, Cu, and Zn. Hydrothermal quartz contains several micrometer-sized mica-based minerals (Fe^{2+}), with traces of Cr, Mn, Cu, and Zn. In Ca-rich particles, Cr, Mn, Fe, Cu, and Zn are also detected.

In quartzite, impurities are often co-located along grain boundaries, albeit with few consistent trends. Ca, Ti, and Fe can be found with traces of K, Cu, and/or Zn. Ti-rich clusters often contain Fe, but several other Fe-rich particles do not contain Ti. Ca-rich particles contain Fe but not necessarily Ti. A higher-resolution μ-XRF image of a grain boundary (Figure 5) shows how Fe distributes along the topology of a typical grain boundary; Ti forms a round particle embedded in Fe; Ca spreads uniformly along the grain boundary and has higher concentration in proximity of the Ti particle.

In the pine woodchip, diffused Fe, Ti, and Ca are co-located along wood veins (Figure 3). In the eucalyptus charcoal, a few particles containing Ca and Fe are observed. The mixed-wood sample has an abundance of particles with Ca, Ti, and Fe co-located.

4. DISCUSSION

Although the precise concentrations, oxidation states, and distributions of impurities may vary considerably within quartz deposits and wood sources, we believe the trends reported in this discussion to be generally applicable to a wide range of raw feedstock materials.

The majority of impurities in raw feedstock materials are observed in the form of distinct particles. This is especially true of the Si-bearing feedstock materials, wherein particles are often present at grain boundaries. This conclusion can be inferred from the good quantitative agreement between μ-XRF, which measures impurity concentrations in distinct particles, and ICP-MS, which measures total bulk impurity concentrations (Figure 6a). The preponderance of impurities in particles is consistent with reported low solid solubilities of impurity point defects in SiO_2 [13–15] and with electronic incompatibilities between impurity atoms and the host matrix [35]. The diffusion of Fe and Ca towards the grain boundaries of quartz has previously been described [13,14]; Ti is also reported to diffuse in quartz, however, to a lesser degree [13,14,36,37]. Additionally, some of the detected particles with high melting points are grain sized (e.g., in quartzite), indicating that trapping of inclusions during geological formation is another pathway leading to particles of foreign minerals.

In C-bearing compounds, charcoalization causes a higher concentration of second-phase particles (Figure 3) and an increase in total impurity content (Figure 6b). Although contaminations from handling and from the charcoalization environment are likely responsible, aggregation of pre-existing impurities and/or differences in sample origin (e.g., location in tree) may be contributing factors.

In carbon-bearing feedstocks, the trend of increasing bulk concentration from Ti to Fe to Ca (Figure 6b) can be explained by the fact that biological functions prefer divalent ions followed by ions with higher valence [23]. Although impurity concentrations greatly depend on growth environment as well as tissue location within the tree, ICP-MS analyses confirm that concentration of divalent calcium are greater than divalent and trivalent Fe followed by tetravalent Ti. A greater understanding of plant biology could lead to naturally purified C-bearing raw feedstock sources.

Reported MG-Si impurity concentrations [38] are often equivalent to or higher than the impurity content measured in the raw feedstock materials herein, suggesting that the current carbothermic reduction process may also contribute a significant amount of impurities. Mirroring the purification of crucible lining materials during multicrystalline Si ingot fabrication [39,40], comparable cost-effective reductions in MG-Si impurity content may be achieved from purifying certain furnace components and improving handling protocols.

The observation of distinct particles in raw feedstock materials, often at structural defects, invites conjecture of novel purification processes that exploit this "natural gettering" phenomenon. Direct introduction into a metallurgical furnace results in the homogenization of feedstock and impurities, despite the initial phase separation occurring during natural geological formation or charcoal production. Physical and chemical processes could separate the impurity particles from the quartz-bearing and carbon-bearing host matrices prior to the carbothermic reduction beyond simple acid leaching [41]. For example, selective fragmentation along grain boundaries before acid leaching could drastically reduce impurity content, despite the challenge of the liberated impurity grain size and the quartz fines produced.

5. CONCLUSIONS

Using synchrotron-based microprobe techniques, we analyze microscopic distributions and oxidation states of impurities in silicon-bearing and carbon-bearing feedstock materials used in the photovoltaic industry. Within silicon-bearing compounds, comparison between quantitative μ-XRF and ICP-MS suggests that the majority of Fe, Ti, and Ca impurities are present in distinct micrometer-sized or sub-micrometer-sized minerals, frequently located at structural defects such as grain boundaries. Although the chemical states of impurities vary, they are generally oxidized (e.g., Fe^{2+}, Fe^{3+}). Impurity concentrations are directly correlated to the geological type of quartz; pegmatitic and hydrothermal quartz have fewer impurities than quartzite. Particles containing Cr, Mn, Fe, Ni, Cu, K, and/or Zn are also detected.

In all carbon-bearing compounds (raw wood and charcoals), Ca is typically diffused uniformly following the veins. In pine wood, Fe and Ti are also diffused uniformly. In contrast, charcoal samples can contain

particles of Fe, Ti, and/or Ca. The overall impurity content in the pine charcoal sample is higher than in the pine woodchip, suggesting that the charcoalization process introduces unintentional contamination.

We postulate that a deeper understanding of impurities, their distribution, and oxidation states may enable the development of novel defect engineering or impurity removal techniques at the starting stage of the refining process. Natural processes leading to impurity segregation and aggregation described in this study should be exploited further: selective cleaning of preferred segregation locations or other physical, chemical, and biological methods could enhance current practice.

ACKNOWLEDGEMENTS

The authors thank B Monsen, SINTEF Materials and Chemistry, Trondheim, Norway, for supplying the C-bearing compounds and insightful discussions. C Francis is acknowledged for helpful geological discussions and S Hudelson for experimental support. M Islam at Metron Tech, Burlingame, CA, is acknowledged for ICP-MS analyses and S Woods for insightful ICP-MS discussions. MA Marcus and B Lai are thanked for experimental support at the Advanced Light Source and Advanced Photon Source, respectively.

Support for this research was provided by the US Department of Energy, under contract number DE-FG36-09GO19001, through the generous support of Doug Spreng and the Chesonis Family Foundation and the BASIC Project, Norwegian Research Council, under contract number 191285/V30. S.B. acknowledges the support of the Leiv Eiriksson mobility program through the Norwegian Research Council. BKN acknowledges the support of the Claire Boothe Luce Foundation. The Advanced Light Source and Advanced Photon Source are supported by the Director, Office of Science, Office of Basic Energy Sciences, of the US Department of Energy under Contracts DE-AC02-05CH11231 and DE-AC02-06CH11357, respectively.

REFERENCES

1. Davis JR, Jr., Rohatgi A, Hopkins RH, *et al*. Impurities in silicon solar cells. *IEEE Transactions on Electron Devices* 1980; **27**: 677–687.
2. Pizzini S. Towards solar grade silicon: challenges and benefits for low cost photovoltaics. *Solar Energy Materials and Solar Cells* 2010; **94**: 1528–1533.
3. Bishop JW. Microplasma breakdown and hot-spots in silicon solar cells. *Solar Cells* 1989; **26**: 335–349.
4. Kwapil W, Gundel P, Schubert MC, *et al*. Observation of metal precipitates at prebreakdown sites in multicrystalline silicon solar cells. *Applied Physics Letters* 2009; **95**: 232113.
5. Hofstetter J, Lelièvre JF, del Cañizo C, Luque A. Acceptable contamination levels in solar grade silicon: from feedstock to solar cell. *Materials Science and Engineering B* 2009; **159–160**: 299–304.
6. Braga AFB, Moreira SP, Zampieri PR, Bacchin JMG, Mei PR. New processes for the production of solar-grade polycrystalline silicon: a review. *Solar Energy Materials and Solar Cells* 2008; **92**: 418–424.
7. Weber ER. Transition metals in silicon. *Applied Physics A: Materials Science & Processing* 1983; **30**: 1–22.
8. Coletti G, Kvande R, Mihailetchi VD, Geerligs LJ, Arnberg L, Ovrelid EJ. Effect of iron in silicon feedstock on p- and n-type multicrystalline silicon solar cells. *Journal of Applied Physics* 2008; **104**: 104913.
9. Graff K. *Metal impurities in silicon-device fabrication*. Springer-Verlag: Berlin Heidelberg, 1995.
10. Ceccaroli B, Lohne O. Solar Grade Silicon Feedstock. In *Handbook of Photovoltaic Science and Engineering*, Luque A, Hegedus S (eds). Wiley: Chichester, 2003.
11. Petter K, Djordjevic-Reiss J, Hoffmann V, *et al*. NAA results for UMG-Si from different sources and qualities. *Proceedings of the Workshop on Arriving at well-founded SoG silicon feedstock specifications, Crystal Clear Project*, Amsterdam, 2008
12. Martin C, Ndzogha C, Morin F, Bouche J-B, Rancoule G. Detrimental effect of alkaline impurities on fused silica crucible during multi-crystalline ingot growth. *Proceedings of the 3rd International Workshop on Crystalline Silicon Solar Cells (CSSC-3)*, Trondheim, Norway, 2009
13. Larsen RB, Henderson I, Ihlen PM, Jacamon F. Distribution and petrogenetic behaviour of trace elements in granitic pegmatite quartz from South Norway. *Contributions to Mineralogy and Petrology* 2004; **147**: 615–628.
14. Larsen RB, Jacamon F, Kronz A. Trace element chemistry and textures of quartz during the magmatic hydrothermal transition of Oslo Rift granites. *Mineralogical Magazine* 2009; **73**: 691–707.
15. Larsen RB, Polvé M, Juve G. Granite pegmatite quartz from Evje-Iveland: trace element chemistry and implications for high-purity quartz formation. *Norges Geologiske Undersøkelse Bulletin* 2000; **436**: 57–65.
16. Sørensen B, Larsen R. Coupled trace element mobilisation and strain softening in quartz during retrograde fluid infiltration in dry granulite protoliths. *Contributions to Mineralogy and Petrology* 2009; **157**: 147–161.
17. Monsen BE, Grønli M, Nygaard L, Tveit H. The use of biocarbon in Norwegian ferroalloy production.

Proceedings of the INFACON 9, Quebec, Canada, 2001; 268–276.
18. Monsen BE, Ratvik AP, Lossius LP. Charcoal in anodes for aluminium production. *Proceedings of the Light Metals 2010—TMS 2010 Annual Meeting and Exhibition, February 14, 2010–February 18, 2010*, Seattle, WA, United States, 2010; 929–934.
19. McHugo SA, Thompson AC, Flink C, *et al*. Synchrotron-based impurity mapping. *Journal of Crystal Growth* 2000; **210**: 395–400.
20. Buonassisi T, Istratov AA, Marcus MA, *et al*. Local measurements of diffusion length and chemical character of metal clusters in multicrystalline silicon. *Solid State Phenomena* 2005; **108–109**: 577–584.
21. Marcus MA. X-ray photon-in/photon-out methods for chemical imaging. *Trends in Analytical Chemistry* 2010; **29**: 508–517.
22. Manceau A, Marcus MA, Tamura N. Quantitative speciation of heavy metals in soils and sediments by synchrotron X-ray techniques. *Reviews in Mineralogy and Geochemistry* 2002; **49**: 341–428.
23. Berglund A, Brelid H, Rindby A, Engstrom P. Spatial distribution of metal ions in spruce wood by synchrotron radiation microbeam X-ray fluorescence analysis. *Holzforschung* 1999; **53**: 474–480.
24. Buonassisi T, Istratov AA, Peters S, *et al*. Impact of metal silicide precipitate dissolution during rapid thermal processing of multicrystalline silicon solar cells. *Applied Physics Letters* 2005; **87**: 1–3.
25. Buonassisi T, Istratov AA, Pickett MD, *et al*. Chemical natures and distributions of metal impurities in multicrystalline silicon materials. *Progress in Photovoltaics: Research and Applications* 2006; **14**: 512–531.
26. Marcus MA, MacDowell AA, Celestre R, *et al*. Beamline 10.3.2 at ALS: a hard X-ray microprobe for environmental and materials sciences. *Journal of Synchrotron Radiation* 2004; **11**: 239–247.
27. Cai Z, Lai B, Yun W, *et al*. Performance of a high-resolution X-ray microprobe at the Advanced Photon Source. *AIP Conference Proceedings* 2000; **521**: 31–34.
28. Mantler M, Willis JP, Lachance GR, *et al*. Quantitative Analysis. In *Handbook of Practical X-Ray Fluorescence Analysis*, Burkhard B, Kanngiesser B, Langhoff N, Wedell R, Wolff H (eds). Springer-Verlag: Berlin Heidelberg, 2006; 309–410.
29. Kraft S, Stuempel J, Becker P, Kuetgens U. High resolution X-ray absorption spectroscopy with absolute energy calibration for the determination of the absorption edge energies. *The Review of Scientific Instruments* 1996; **67**: 681–687.
30. Kelly SD, Hesterberg D, Ravel B. Analysis of soils and minerals using X-ray absorption spectroscopy. In *Methods of Soil Analysis, Part 5—Mineralogical Methods*, Ulery AL, Drees LR (eds). Soil Science Society of America: Madison, WI, 2008; 367–464.
31. Marcus MA, Westphal AJ, Fakra SC. Classification of Fe-bearing species from K-edge XANES data using two-parameter correlation plots. *Journal of Synchrotron Radiation* 2008; **15**: 463–468.
32. Wilke M, Partzsch GM, Bernhardt R, Lattard D. Determination of the iron oxidation state in basaltic glasses using XANES at the K-edge. *Chemical Geology* 2005; **220**: 143–161.
33. Farges F, Brown GE, Rehr JJ. Ti K-edge XANES studies of Ti coordination and disorder in oxide compounds: Comparison between theory and experiment. *Physical Review B* 1997; **56**: 1809.
34. Waychunas GA. Synchrotron radiation XANES spectroscopy of Ti in minerals: effects of Ti bonding distances, Ti valence, and site geometry on absorption edge structure. *American Mineralogist* 1987; **72**: 89–101.
35. Hiraga T, Anderson IM, Kohlstedt DL. Grain boundaries as reservoirs of incompatible elements in the Earth's mantle. *Nature* 2004; **427**: 699–703.
36. Cherniak DJ, Watson EB, Wark DA. Ti diffusion in quartz. *Chemical Geology* 2007; **236**: 65–74.
37. Wark D, Watson E. TitaniQ: a titanium-in-quartz geothermometer. *Contributions to Mineralogy and Petrology* 2006; **152**: 743–754.
38. Murray JP, Flamant G, Roos CJ. Silicon and solar-grade silicon production by solar dissociation of Si3N4. *Solar Energy* 2006; **80**: 1349–1354.
39. Olsen E, Øvrelid EJ. Silicon nitride coating and crucible—effects of using upgraded materials in the casting of multicrystalline silicon ingots. *Progress in Photovoltaics: Research and Applications* 2008; **16**: 93–100.
40. Kvande R, Arnberg L, Martin C. Influence of crucible and coating quality on the properties of multicrystalline silicon for solar cells. *Journal of Crystal Growth* 2009; **311**: 765–768.
41. Lee K, Yoon Y, Jeong S, Chae Y, Ko K. Acid leaching purification and neutron activation analysis of high purity silicas. *Journal of Radioanalytical and Nuclear Chemistry* 2009; **282**: 629–633.

Using synchrotron based analytical microprobe techniques, we determine micrometer scale elemental composition, spatial distribution, and oxidation state of impurities in quartz and carbon bearing raw feedstock materials used in the photovoltaic industry. In both feedstocks, impurities are predominantly found clustered and in an oxidized form.